Malayaite Ceramic Pigments: a Combined Optical Spectroscopy and Neutron/X-ray Diffraction Study

Giuseppe Cruciani[1], Michele Dondi[2], Matteo Ardit[1], Teodora Stoyanova Lyubenova[3], Juan B. Carda[3], Francesco Matteucci[2], Anna L. Costa[2]

[1]*Department of Earth Sciences, University of Ferrara, Via Saragat 1, 44100 Ferrara, Italy*
[2]*ISTEC-CNR, Institute of Science and Technology for Ceramics, Via Granarolo 64, 48018 Faenza, Italy*
[3]*Dept of Inorganic and Organic Chemistry, University Jaime I, Campus Riu Sec, 12071 Castellón, Spain*

Abstract. Ceramic pigments based on the Cr-doped malayaite structure were synthesized by solid state reaction and characterized by optical spectroscopy and combined X-ray and neutron powder diffraction in order to elucidate the still unclear chromium substitution mechanisms. The results show that coloration is actually due to simultaneous occurrence of Cr^{4+} and Cr^{3+} ions in the crystal lattice. Spectroscopy data confirm that Cr^{4+} is replacing Sn^{4+} in the octahedral site and, in minor amount, Si^{4+} in the tetrahedral site. In addition, neutron powder diffraction data suggest that Cr^{3+} substitution for octahedral Sn^{4+} is charge balanced by formation of oxygen vacancies with no preference over the different oxygen sites. Upon incorporation of Cr ion, the SnO_6 octahedra exhibit an off-centre displacement of central cation which in turn induces a rearrangement of both the octahedral and tetrahedral coordination shells.

Key-words: ceramic pigment, crystal structure, malayaite, neutron diffraction, optical spectroscopy, X-ray diffraction.

1. Introduction

Malayaite ($CaSnOSiO_4$) is a rare calcium and tin silicate containing isolated SiO_4 tetrahedra with an additional oxygen (titanite group) usually found in skarns [1]. Its crystal structure, first solved by Higgins and Ribbe [2], consists of corner-sharing SnO_6 octahedra, forming slightly kinked chains parallel to *a*, which are mutually connected via SiO_4 tetrahedra, so within the SnO_6-SiO_4 framework irregular CaO_7 polyhedra are defined [2-6]. Malayaite crystallizes with monoclinic lattice and is topologically identical with titanite ($CaTiOSiO_4$), but truly isostructural only with the high temperature polymorph of chemically pure titanite [3-7]. The $CaSnOSiO_4$-$CaTiOSiO_4$ join investigation showed that a small substitution (10 mol%) of Sn changes the titanite symmetry from $P2_1/a$ to $A2/a$ [3].
Malayaite is an important ceramic pigment, being the only, whenever doped with chromium, to develop peculiar deep burgundy to pink shades that are stable in a wide range of temperatures, although its colouring performance varies sensibly in different ceramic glazes [8-10]. However, it is noteworthy for its inherent difficulty in making reproducible pigment shades, originated by uncontrolled solid state reactions between raw materials [8-9]. As a matter of fact, the malayaite pigment colour may change from lot to lot, depending on several factors: firing time and temperature [11-13], occurrence of secondary phases [13-14], type and amount of mineralizers [11-12, 14-15] or co-dopants [8, 11, 16], different methods of mixing precursors, such as sol-gel, coprecipitation or spray pyrolisis [15, 18].
The pigment was originally designed assuming chromium incorporated in the malayaite lattice as Cr^{3+} [8, 12, 16]. However, this assumption does not match the optical properties [17] and has been recently suggested, based on spectroscopic data only, that chromium is

mostly in the tetravalent state [18] mainly replacing Sn^{4+} in the octahedral site, even though minor Cr^{4+} substitutes Si^{4+} in the tetrahedral site [19].

On the other hand, the mechanism by which Cr is incorporated in the malayaite structure is still unclear. This is partly due to the three possible oxidation states of Cr hosted in this structure (Cr^{3+}, Cr^{4+}, and Cr^{5+}), as partially supported by spectroscopic analyses [19, 21-22]. In the case of Cr^{3+}, a substitution in the octahedral site, such as $2Sn^{4+} + 4O^{2-} \rightarrow 2Cr^{3+} + 3O^{2-} + V_o''$, can be envisaged leading to formation of oxygen vacancies (V_o), which would likely occur at the oxygen site bridging two octahedra. In the titanite structure this oxygen site (O1) is known to be slightly underbonded compared to the other oxygen ions and is commonly replaced by monovalent anions, such as F or OH [2, 23]. Therefore a vacancy in the O1 site, although never reported before, cannot be ruled out as a local charge balance mechanism. A second incorporation mechanism, involving Cr^{4+}, can be suggested as the isovalent substitution in both tetrahedral ($Si^{4+} \rightarrow Cr^{4+}$) and octahedral ($Sn^{4+} \rightarrow Cr^{4+}$) sites does not require oxygen vacancies. It is likely that all these mechanisms coexist to some extent, making their recognition not straightforward by spectroscopic methods alone [19, 21-22].

The aim of the present study is a better understanding of the chromium incorporation mechanisms in malayaite by means of combined neutron/X-ray diffraction and optical spectroscopy analyses.


2. Experimental

2.1. Design of pigments and synthesis procedure

Cr-doped malayaite pigments were designed according to the following two strategies: a series of five samples, based on the assumption that Cr^{4+} replaces Si^{4+} in tetrahedral sites. The resulting nominal compositions are (Table 1):

$CaSnSi_{1-x}Cr_xO_4O$
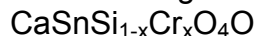
where x = 0.018, 0.025, 0.050, 0.075, 0.100 a.p.f.u. (atoms per formula unit). Samples are named S18, S25, S50, S75 and S100, respectively. One sample was designed assuming that Cr^{3+} replaces Sn^{4+} in the octahedral site and the exchange is charge balanced by formation of oxygen vacancies. The resulting composition, named T18, is:

$CaSn_{1-y}Cr_ySiO_4O$
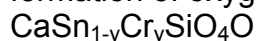
where y = 0.018 a.p.f.u.

Both series were synthesized via solid state reaction by using reagent-grade (purity >99.5%) $CaCO_3$ (Merck, 99%), Cr_2O_3 (J.T Baker, 99%), SiO_2 (Strem Chemical, 99.5%), and SnO_2 (Panreac, 99%) as precursors. The raw materials were mixed and homogenized by stirring in acetone by a ball mill, then dried in oven at 100°C. Dried powders were calcined in electric kiln at 1300 °C for 4 h, in static air and unsealed alumina crucibles.

2.2. Optical spectroscopy

Diffuse reflectance spectroscopy (DRS) was performed by a Perkin Elmer λ19 spectrophotometer (300-1400 nm range, 0.03 nm step size, $BaSO_4$ integrating sphere, $BaSO_4$ pellet as white reference material). Reflectance (R_∞) was converted to absorbance (K/S) by the Kubelka-Munk equation: $K/S=2(1-R_\infty)\cdot(2R_\infty^{-1})$ [24]. Absorbance bands in the 7000-27000 cm^{-1} range were deconvoluted constraining full width at half maximum (FWHM) to ≤ 3000 cm^{-1} (PFM, OriginLab) in order to get energy (centroid), splitting (FWHM) and optical density (area) of 13 gaussian peaks. The experimental errors, including background correction and reproducibility, are ~2% (energy), ~5% (splitting) and ~10% (optical density). Every band was attributed by fitting its energy in the relevant Tanabe-Sugano diagrams: (d^2 for Cr^{4+} in octahedral coordination, d^3 for sixfold-coordinated Cr^{3+}, and d^8 for tetrahedrally-coordinated Cr^{4+}) and determining both crystal field strength *10Dq* and the interelectronic repulsion Racah *B* parameter by spin-allowed

transitions [25-27]. Band attribution was verified calculating expected band energies on the basis of 10Dq and B values [24, 27-28]. The nephelauxetic ratio β was calculated as $\beta=B/B_0$, where B is experimental and B_0 is the value of the free ion [27, 29].

2.3. Diffraction

X-ray powder patterns were collected with a Bruker D8 Advance automated diffractometer, equipped with a Si(Li) solid state detector (Sol-X) set to detect CuK$\alpha_{1,2}$ radiation. Scans were recorded in the 15–130° 2θ range with 0.02° 2θ steps and 10 s counting time per step. The neutron powder diffraction experiments were performed at the Institut Laue Langevin (ILL, Grenoble, France). Data were collected at room-temperature using the high-resolution two-axis diffractometer at the D2B station [30] with a wavelength of 1.59432 Å. This instrument is characterized by a high take-off angle (135°) for the monochromator (Ge 335), which has a relatively large mosaic spread of 20' to compensate for the corresponding intensity loss. It is 300 mm high, focusing vertically onto about 50 mm; this large incident vertical divergence is matched by 200 mm high detectors and collimators. A complete diffraction pattern was obtained after about 100 steps of 0.025° 2θ, since the 64 detectors are spaced at 2.5° intervals, and the scans were repeated to improve statistics. Each sample was collected for about 6 hours.

The Rietveld refinements of X-ray and neutron powder diffraction patterns were accomplished using the GSAS and EXPGUI packages [31-32]. For the X-ray data, the diffraction peak profiles were modeled by a pseudo-Voigt function with one Gaussian and two Lorentzian broadening coefficients plus an asymmetry contribution. Besides the Chebyshev polynomial coefficients to model the background, all refinements included a scale factor, the profile coefficients and the cell parameters for each phase present. The atomic coordinates, site occupancy factors, and atomic displacement parameters (ADPs) were refined only for the malayaite structure. The refinement was carried out in the non-standard space group *A*12/*a*1, starting from the model of Higgins and Ribbe [2]. For the neutron data, three Gaussian and one Lorentzian coefficients of the pseudo-Voigt function were varied, plus the asymmetry contribution. The refinement strategy was the same as described above for X-rays with the only difference that the occupancy of oxygen sites of malayaite structure was also refined. A third group of refinements were performed using both the X-ray and neutron datasets combined in the same refinement. The structural results reported on Table 1 and Table 6 are those obtained from these latter group of refinements. Rietveld analysis of neutron or combined X-rays/neutron powder diffraction data is a technique particularly suitable for detecting the occurrence of significant anion vacancies, because the oxygen site occupancy can be reliably estimated during structural refinement. Furthermore, the contrast between neighboring atomic species located within the same cationic sites can be enhanced in the occupancy refinements. This allows to better constrain the previously mentioned hetero- and iso-valent substitutions together with the evaluation of polyhedral distortion factors as a function of Cr-doping. A representative Rietveld fit resulting from our refinements is illustrated in Figure 1.

3. Results and discussion

3.1. Phase composition

The major phase occurring in all samples is the monoclinic malayaite. As reported in Table 1, the amount of this phase varies from a minimum of 92% (sample S25) to a maximum of 94% (sample S75). Minor phases represent unreacted precursors, such as cassiterite (SnO_2) and α-cristobalite (SiO_2); eskolaite (Cr_2O_3) is present only in the sample with the maximum amount of chromium in the batch (S100).

3.2. Optical properties

The Cr-doped malayaite exhibits complex optical spectra with several weak bands in the near infrared and a steep slope, with onset at ~15000 cm^{-1}, culminating at ~19000 cm^{-1} and gradually decreasing towards the UV region (Fig. 2a). The occurrence of two distinct low-absorbance regions, transmitting respectively the red-orange light and to a lesser extent the blue-violet wavelengths, is able to explain the peculiar burgundy-pink colour of malayaite pigments [33]. A similar optical fingerprint, found in as-grown crystals of Cr-doped aluminates, silicates and germanates, is attributed to the superposition of Cr^{3+} and Cr^{4+} contributes [34-36]. The maximum colour strength was found for the sample S50, corresponding to a nominal Cr amount of 0.05 a.p.f.u., in good agreement with literature indicating best doping for Cr = 0.04 [11, 15, 17].

Optical spectra were interpreted as resulting from the coexistence of the following *d-d* electronic transitions (Fig. 2b):

i) Cr^{3+} in octahedral environment, with t_2^3 ground state $^4A_{2g}(^4F)$, exhibits two intense, parity-forbidden and spin-allowed transitions to the t_2^2e excited state: $^4T_{2g}(^4F)$ at ~17500 cm^{-1} and $^4T_{1g}(^4F)$ at ~23000 cm^{-1}. Furthermore, two tiny peaks at ~11000 and ~13000 cm^{-1} are attributable to the doubly-forbidden transitions ^2E_g and $^2T_{1g}(^2G)$, respectively;

ii) Cr^{4+} in sixfold coordination has a t_2^2 ground state $^3T_{1g}(^3F)$ with two Laporte-forbidden and spin-allowed transitions to t_2e: $^3T_{2g}(^3F)$ at ~19200 cm^{-1} and $^3T_{1g}(^3P)$ at ~26000 cm^{-1}. A weak band at ~8000 cm^{-1} is due to the overlapping contributions of spin-forbidden transitions ^1E_g and $^1T_{2g}(^1D)$;

iii) tetrahedrally-coordinated Cr^{4+} is characterized by three spin-allowed transitions from the t_2^2 ground state $^3A_2(^3F)$: $^3T_2(^3F)$, split in two bands at ~8900 and ~10300 cm^{-1}, and $^3T_1(^3F)$ at ~14500 cm^{-1} are to the t_2e level, while $^3T_1(^3P)$ is a two-electron transition (e^2) occurring at ~21000 cm^{-1}. Further two weak bands, observed at energies close to 11000 and 16000 cm^{-1}, are referable to the spin-forbidden transitions $^1A_1$ and $^1T_2(^1G)$, respectively.

Accordingly, the optical spectra deconvolution consisted of thirteen bands, whose energy, splitting and optical density are summarized in Tables 2-4.

The above attributions are consistent with crystal field theory, as band energies reasonably fit (generally within ±300 cm^{-1}) both calculated values (Tables 2-4) and literature data on oxidic structures [26-29, 34-38]. The main discrepancies, in the order of 1000 cm^{-1}, concern the $^3T_1(^3P)$ transition of Cr^{4+} in tetrahedral coordination and the spin-forbidden transitions of trivalent chromium.

The main optical parameters, achieved for the first time for Cr-doped malayaite, are summarized in Table 5. The crystal field strength values of all the chromophore ions are slightly higher than expected on the basis of the mean Sn-O and Si-O distances. In the point charge assumption of the crystal field theory, an inverse dependence of 10Dq is predicted on the fifth power of the mean metal-oxygen distance [26-29]. This likely implies a different local environment of chromium ions in the malayaite lattice with respect to other oxidic structures without significant changes of covalent degree of Cr-O bond, as the interelectronic repulsion Racah B parameters and the correspondent nephelauxetic ratios fall within the variation range found in the literature [26-29, 34-40]. In particular, the 10Dq value of tetrahedrally-coordinated Cr^{4+} is around 10100 cm^{-1}, therefore higher than in YAG, calcium germanate or forsterite, where values in the 9000-9600 cm^{-1} range correspond to <Cr-O> of about 1.75-1.77 Å [38-39]. In the case of sixfold coordinated Cr^{4+}, the crystal field strength in yttrium stannate pyrochlores (~19800 cm^{-1}) is close to that in malayaite (~20200 cm^{-1}) suggesting a slightly shorter mean Cr-O distance [40]. The 10Dq value for Cr^{3+} in octahedral coordination (~17400 cm^{-1}) would imply a local <Cr-O> distance around 1.96 Å, which is shorter than expected taking into account the relatively large space

available in SnO_6 octahedra, since the ionic radius of Sn^{4+} (0.69 Å) is significantly longer than that of Cr^{3+} (0.615 Å) [41].

The optical density of Cr^{4+} spin-allowed bands is much higher in sixfold than in fourfold coordination, besides the probability of electronic transitions in non centrosymmetric sites, like tetrahedral ones, being higher by a factor 10 to 50 [26-27]. This fact confirms that Cr^{4+} replaces Si^{4+} in very small amount and most chromium ions are accommodated in substitution of Sn^{4+} [19].

3.3. Crystal structure of malayaite

The incorporation of Cr affects malayaite unit cell dimensions (Table 1): the volume shows a relatively small variation from 388.9 $Å^3$ to 389.3 $Å^3$, the latter value being very close to what reported in the literature for undoped malayaite [4, 42]. However, these changes do not scale regularly with the chromium percentage of batches, since the amount of Cr actually incorporated into the malayaite lattice is different from what designed. This is due to the occurrence of secondary phases, which can host Cr inside their structure, i.e. cassiterite (4-6 wt.%) and eskolaite (approximately 1 wt.% in sample S100). Nevertheless, account must be taken that the actual solubility of chromium inside the cassiterite lattice is as low as 0.02 a.p.f.u. [43-44]. The picture is further complicated by the occurrence of various Cr valences at different crystallographic sites, as indicated by optical spectroscopy.

Considering that most chromium is accommodated in the octahedral site, as inferred from optical data, this substitution implies a significant difference of ionic radii, being Cr^{4+} 0.55 Å, Cr^{3+} 0.615 Å, Sn^{4+} 0.69 Å in sixfold coordination [41]. Thus an increasing Cr amount in the malayaite structure shall be denoted by the proportional decreasing of unit cell volume. Therefore, the Cr fraction into the pigments under investigation is expected to be rearranged in the following decreasing order: T18 > S100 > S50 > S18 > S75 > S25. On the basis of this setting, it is noteworthy that the *a*-, *b*-, and *c*-axis lengths scale linearly and positively with the raising of the unit cell volume (see Table 1). This is expected when the mean ionic radius of cations in the octahedral site decreases along with the substitution of Cr for Sn. On the other hand, the value of β angle is almost constant (113.3° on average).

The mean metal-oxygen distances of the three structural sites vary according to the following trends: <Ca-O> and <Si-O> increase with the raising unit cell volume, while <Sn-O> decreases (Fig. 3). This trend apparently contradicts the prediction that chromium replaces tin in the octahedral site, since the reduced mean ionic radius is expected to reflect on a shorter metal-oxygen distance. An explanation can be seen in the anisotropic variation of the single Sn-O distances (Fig. 4). In fact, plotting the Sn-O1, Sn-O2 and Sn-O3 bond distances versus the unit cell volume, two inverse trends arise, implying that the SnO_6 octahedron turns more and more distorted as the unit cell volume turns smaller.

The reason for such distortion is that chromium is likely accommodated inside that octahedron not exactly at the same special position of tin (½, ½, 0; i.e. the ideal site centre) but it is slightly shifted in an off-centre position, bisecting the O2-Sn-O3 angle on the plane formed by the same oxygens. As a consequence, the octahedral site exhibits a flattened shape with two couples of long distances, Sn-O2 and Sn-O3, and a couple of short distances with apical oxygens, Sn-O1. This flattening is enhanced with increasing the Cr/Sn ratio, suggesting that the octahedral central cation moves closer to the two apical oxygens (O1) and away from the other two coordinating oxygens (O2 and O3) when Sn is replaced by Cr^{4+} and Cr^{3+} ions. An off-centre position of Cr^{4+} in the octahedral site is able to justify the anomalously high optical density of its bands, which is permitted by its non-centrosymmetric location, which relaxes the Laporte selection rule [27-29]. Such anomalous optic efficiency cannot be accounted for an intervalence charge transfer

mechanism (IVCT, e.g. $Cr^{3+} \leftrightarrow Cr^{4+}$) because the metal-metal distances in malayaite (approximately 3.6 Å for Sn-Sn and 3.3 Å for Si-Sn) are too long with respect to usual distances observed in IVCT (2.6-3.1 Å) [26,45].

The chromium ion displacement induces in turn a structural rearrangement within the SiO_4 tetrahedra and the CaO_7 polyhedra: as the Sn-O2 bond distance increases, the Si-O2 decreases (Fig. 5a); a similar relationship occurs between Sn-O3 and Ca-O3 (Fig. 5b). Both these inverse relationships occur to comply with the local charge requirements at the oxygen sites.

One of the goals of the present study was to verify if the occurrence of oxygen vacancies could be found as an active mechanism to achieve the charge balance after replacement of Sn^{4+} by Cr^{3+}. Comparison with F- and OH-substituted titanites suggests that oxygen vacancies, if any, would be preferentially located at the O1 site [2, 23]. The oxygen occupancy fractions refined using neutron data vary in the 0.94(1)-0.97(1) range, without any preference among the three non-equivalent oxygen sites (O1, O2, O3) in malayaite. This suggests an overall occurrence of 6% oxygen vacancies.

4. Conclusions

The present optical spectroscopy and combined X-ray and neutron powder diffraction study of Cr-doped malayaite reveal the simultaneous occurrence of Cr^{4+} and Cr^{3+} ions in the crystal lattice, which is the cause of the peculiar coloration of these pigments. Spectroscopic data show that Cr^{4+} is predominantly replacing Sn^{4+} in the octahedral site, but a small amount of Cr^{4+} is substituting for Si^{4+} in the tetrahedral site. The combined X-ray and neutron powder diffraction refinements suggest that Cr^{3+} is accommodated into SnO_6 octahedra likely by an oxygen vacancy mechanism with no preference for any O site. Chromium ions are allocated by an off-centre displacement with respect to the octahedral site central position, inducing a rearrangement of both octahedral and tetrahedral coordination shells. This leads to enhanced site distortion for increasing Cr substitution. Furthermore, Cr ions reside, due to their off-centre location, in a non-centrosymmetric coordination which, relaxing the Laporte selection rule, makes it possible the high optical density of d-d- transitions, particularly the Cr^{4+} absorption bands.

The well-known difficult colour reproducibility of malayaite pigments may be connected with changes in both valence and distribution of chromium into the octahedral and tetrahedral sites. These variables also explain why the total Cr content is not a factor influencing the color properties. In fact, the best magenta hues stem from a compromise, hard to be managed in industrial manufacturing conditions, involving high concentration of Cr^{4+} in octahedral coordination, which ensures the desired absorption of green light, together with low concentration of both Cr^{4+} in tetrahedral coordination and Cr^{3+}, whose optical bands are deleterious for the burgundy coloration, since absorb red-orange and blue-violet wavelengths, respectively. In the present study, the best compromise was found to be the sample S50, where 0.5 apfu of chromium are mainly represented by Cr^{4+} in sixfold coordination.

Acknowledgements

References

[1]   J.B. Higgins, P.H. Ribbe, Am. Miner. 61 (9-10) (1976) 878.
[2]   J.B. Higgins, P.H. Ribbe, Am. Miner. 62 (7-8) (1977) 801.

[3]   M. Kunz, D. Xirouchakis, Y.B. Wang, J.B. Parise, D.H. Lindsley, Schweiz. Miner. Petrog. 77 (1) (1077) 1.
[4]   L.A. Groat, S. Kek, U. Bismayer, C. Schmidt, H.G. Krane, H. Meyer, L. Nistor, G. VanTendeloo, Am. Miner. 81 (5-6) (1996) 595.
[5]   N.N. Eremin, V.S. Urusov, V.S. Rusakov, O.V. Yakubovich, Crystallogr. Rep. 47 (5) (2002) 759.
[6]   D. Niemeier, H. Mehner, U. Bismayer, K.D. Becker, Phys. Status Solidi B 211 (2) (1999) 581.
[7]   U. Bismayer, M. Zhang, L.A. Groat, E.K.H. Salje, H.W. Meyer, Phase Transit. 68 (3) (1999) 545.
[8]   R.A. Eppler, Am. Ceram. Soc. Bull. 66 (1987) 1600.
[9]   R.A. Eppler, Kirk-Othmer Encyclopaedia of Chemical Technology, 4th ed., vol. 6, 1992, pp. 877-892.
[10] Escardino, S. Mestre, C. Feliu, P. Jodar, L. Diaz, Brit. Ceram. T. 101 (5) (2002) 213.
[11] V. Harisanov, R.S. Pavlov, I.T. Marinova, V. Kozhukharov, J.B. Carda, J. Eur. Ceram. Soc. 23 (3) (2003) 429.
[12] D.V. Sanghani, G.R. Abrams, P.J. Smith, Brit. Ceram. Trans. J. 80 (6) (1981) 210.
[13] X. Faurel, A. Vanderperre, P. Colomban, J. Raman Spectrosc. 34 (4) (2003) 290.
[14] R. Stefani, E. Longo, P. Escribano, E. Cordoncillo, J.B. Carda, Am. Ceram. Soc. Bull. 76 (9) (1997) 61.
[15] E. Cordoncillo, P. Escribano, G. Monros, M.A. Tena, V. Orera, J.B. Carda, J. Solid State Chem. 118 (1) (1995) 1.
[16] J. Alarcon, P. Escribano, J.J. Gargallo, Brit. Ceram. Trans. J. 83 (3) (1984) 81.
[17] E. López-Navarrete, M. Ocana, J. Eur. Ceram. Soc. 22 (3) (2002) 353.
[18] A.M. Heyns, P.M. Harden, J. Phys. Chem. Solids 60 (2) (1999) 277.
[19] E .López-Navarrete, A. Caballero, V.M. Orera, F.J. Lázaro, M. Ocaña, Acta Mater. 51 (8)(2003) 2371.
[20] M. Kunz, T. Arlt, J. Stolz, Am. Miner. 85 (10) (2000) 1465.
[21] R.S. Pavlov, V.B. Marza, J.B. Carda. J. Mater. Chem. 12 (9) (2002) 2825.
[22] Domenech, F.J. Torres, E.R. de Sola, J. Alarcon. Eur. J. Inorg. Chem. (3) (2006) 638.
[23] B.R. Frost, K.R. Chamberlain, J.C. Schumacher, Chem. Geol. 172 (1-2) (2001) 131.
[24] S. Marfunin, Physics of Minerals and Inorganic Materials. Springer, Berlin/Heidelberg/NewYork, 1979.
[25] Y. Tanabe, S. Sugano, J. Phys. Soc. Jap. 9: (1954) 753.
[26] R.G. Burns, Mineralogical Applications of Crystal Field Theory, 2nd ed., Cambridge University Press, Cambridge, 1993.
[27] A.B.P. Lever, Inorganic Electronic Spectroscopy, 2nd ed., Elsevier, Amsterdam, 1984.
[28] M. Wildner, M. Andrut, C.Z. Rudowicz, in: A. Beran, E. Libowitzky (Eds.), Optical Absorption Spectroscopy in Geosciences. Part I. Basic Concepts of Crystal Field Theory, EMU Notes in Mineralogy, vol. 6, Eötvös University Press, 2004, p. 93.
[29] M. Andrut, M. Wildner, C.Z. Rudowicz, in: A. Beran, E. Libowitzky, (Eds.), Optical Absorption Spectroscopy in Geosciences. Part II. Quantitative Aspects of Crystal Fields, EMU Notes in Mineralogy, vol. 6, Eötvös University Press, 2004, p. 145.
[30] A.W. Hewat, Mater. Sci. Forum 9 (1986) 69.
[31] A.C. Larson, R.B. Von Dreele, General Structure Analysis System (GSAS), Los Alamos National Laboratory Report LAUR 2000, pp. 86.
[32] B.H. Toby, J. Appl. Cryst. 34 (2001) 210.
[33] K. Nassau, The Physics and Chemistry of Color. The Fifteen Causes of Color, 2nd ed. New York: Wiley & Sons, 2001.
[34] R. Feldman, Y. Shimony, Z. Burshtein, Opt. Mater. 24 (1-2) (2003) 333.
[35] Henderson, H.G. Gallagher, T.P.J. Han, M.A. Scott, J. Phys.-Condens. Mat. 12 (8) (2000) 1927.
[36] M. Grinberg, A. Sikorska, A. Sliwinski, J. Barzowska, Y.R. Shen, S.B. Ubizskii, S.S. Melnyk, Phys. Rev. B 67 (4) (2003) 045113.
[37] K. Wissing, M.T. Barriuso, J.A. Aramburu, M. Moreno, J. Chem. Phys. 111 (22) (1999) 10217.
[38] M.F. Hazenkamp, H.U. Gudel, M. Atanasov, U. Kesper, D. Reinen, Phys. Rev. B 53 (5) (1996) 2367.
[39] Reinen, U. Kesper, M. Atanasov, J. Roos, Inorg. Chem. 34 (1) (1995) 184.
[40] F. Matteucci, G. Cruciani, M. Dondi, G. Baldi, A. Barzanti, Acta Mater 55 (7) (2007) 2229.
[41] R.D. Shannon, Acta Crystallogr A 32 (1976) 751.
[42] S. Rath, M. Kunz, R. Miletich, Am. Miner. 88 (2-3) (2003) 293.
[43] Lopez-Navarrete, A.R. Gonzalez-Elipe, M. Ocana, Ceram. Int. 29 (4) (2003) 385.
[44] M.A. Tena, S. Meseguer, C. Gargori, A. Fores, J.A. Badenes, G. Monros, J. Eur. Ceram. Soc. 27 (1) (2007) 215.
[45] M. Lenglet, F. Hochu, S. Music, Solid State Commun. 94 (3) (1995) 211.

Table 1.
Batch and phase composition of pigments, X-ray and neutron diffraction refinement details, and malayaite unit cell parameters.

Sample label	T18	S100	S50	S18	S75	S25
Batch composition (molar ratios)						
$CaSnO(Si_{1-x}Cr_x)O_4$		$x = 0.100$	$x = 0.050$	$x = 0.018$	$x = 0.075$	$x = 0.025$
$Ca(Sn_{1-y}Cr_y)OSiO_4$	$y = 0.018$					
Quantitative phase analysis (% wt.)						
Malayaite	92.5(3)	93.1(4)	92.4(4)	93.1(2)	93.5(4)	91.5(4)
SnO_2 (cassiterite)	4.2(4)	5.3(5)	6.4(5)	5.1(4)	5.3(5)	5.9(5)
SiO_2 (cristobalite)	3.3(9)	0.3(4)	1.2(7)	1.8(7)	1.3(7)	2.6(9)
Cr_2O_3 (eskolaite)	-	1.3(5)	-	-	-	-
Agreement factors and refinement details						
R_{wp} (*XRD*)	0.1366	0.1329	0.1359	0.1223	0.1419	0.1297
R_{wp} (*ND*)	0.0569	0.0597	0.0557	0.0648	0.0540	0.0642
R_p (*XRD*)	0.0940	0.0908	0.0894	0.0850	0.0940	0.0860
R_p (*ND*)	0.0446	0.0470	0.0427	0.0509	0.0421	0.0498
Number of data (*XRD*)	5999	6000	6000	6000	6000	6000
Number of data (*ND*)	2978	2978	2978	2978	2978	2978
R_{Bragg} (*XRD*)	0.0479	0.0549	0.0561	0.0484	0.0543	0.0498
R_{Bragg} (*ND*)	0.0737	0.0655	0.0513	0.0757	0.0752	0.0697
Number of reflections (*XRD*)	675	675	675	675	675	675
Number of reflections (*ND*)	384	384	384	384	384	384
Number of variables	51	118	114	41	114	114
Malayaite unit cell parameters[1]						
a (Å)	7.14752(6)	7.14779(5)	7.14782(6)	7.14891(5)	7.14984(6)	7.15006(5)
b (Å)	8.89003(7)	8.89060(6)	8.89067(7)	8.89119(6)	8.89253(7)	8.89230(6)
c (Å)	6.66497(6)	6.66539(5)	6.66556(6)	6.66634(5)	6.66714(6)	6.66743(5)
β (°)	113.334(1)	113.333(1)	113.337(1)	113.337(1)	113.331(1)	113.333(1)
Unit cell volume(Å³)	388.87	388.93	388.94	389.06	389.24	389.25

[1]Cell parameters as obtained from combined X-ray/neutron refinements

Table 2
Band energy, splitting and optical density of Cr^{4+} in tetrahedral coordination in the malayaite pigments. Electronic transition are referred to in both high symmetry (T_d) and actual point symmetry (C_2) notation.

sample	electronic transitions (T_d)	$^3T_2 (^3F)$	$^3T_2 (^3F)$	$^1A_1 (^1G)$	$^3T_1 (^3F)$	$^1T_2 (^1G)$	$^3T_1 (^3P)$
	electronic transitions (C_2)	^3B	^3A	^1A	^3B	^3A	^3B
T18	energy (measured, cm^{-1})	8870	10380	11790	14680	16180	21060
	energy (calculated, cm^{-1})	*n.d.*	*10240*	*10974*	*14210*	*16347*	*22405*
	band splitting (cm^{-1})	1420	1610	1940	1740	1640	2450
	optical density (a.u.)	380	360	590	660	770	3830
S18	energy (measured, cm^{-1})	9020	10220	11800	14500	16170	21100
	energy (calculated, cm^{-1})	*n.d.*	*10090*	*10993*	*14069*	*16239*	*22141*
	band splitting (cm^{-1})	1090	1540	1550	1700	1820	2200
	optical density (a.u.)	200	310	430	620	830	2850
S25	energy (measured, cm^{-1})	9010	10260	11800	14540	15910	21260
	energy (calculated, cm^{-1})	*n.d.*	*10130*	*11164*	*14165*	*16386*	*22270*
	band splitting (cm^{-1})	1100	1270	1720	1590	1720	2480
	optical density (a.u.)	390	350	560	610	650	4470
S50	energy (measured, cm^{-1})	8970	10310	11040	14580	16000	21230
	energy (calculated, cm^{-1})	*n.d.*	*10160*	*11052*	*14161*	*16341*	*22289*
	band splitting (cm^{-1})	1270	1620	2160	1750	1760	2190
	optical density (a.u.)	390	410	580	650	770	3090
S75	energy (measured, cm^{-1})	9100	10550	11010	14450	16290	21010
	energy (calculated, cm^{-1})	*n.d.*	*10240*	*10541*	*14076*	*16250*	*22284*
	band splitting (cm^{-1})	1440	1450	1340	1820	1880	2160
	optical density (a.u.)	100	140	230	470	470	1600
S100	energy (measured, cm^{-1})	8850	10200	11050	14580	16230	21100
	energy (calculated, cm^{-1})	*n.d.*	*10100*	*10995*	*14080*	*16250*	*22160*
	band splitting (cm^{-1})	1310	1600	1680	1600	1810	2190
	optical density (a.u.)	210	250	570	630	930	2690

Table 3
Band energy, splitting and optical density of Cr^{4+} in octahedral coordination in the malayaite pigments. Electronic transition are referred to in both high symmetry (O_h) and actual point symmetry (C_i) notation.

sample	electronic transitions (O_h)	${}^1E_g+{}^1T_{2g}$ (${}^1D$)	${}^3T_{2g}$ (${}^3F$)	${}^3T_{1g}$ (${}^3P$)
	electronic transitions (C_i)	${}^1A_g$	${}^3A_g$	${}^3A_g$
T18	energy (measured, cm^{-1})	8090	19060	26000
	energy (calculated, cm^{-1})	*8068*	*18835*	*25890*
	band splitting (cm^{-1})	1070	2560	3000
	optical density (a.u.)	210	5380	2100
S18	energy (measured, cm^{-1})	8190	19260	25800
	energy (calculated, cm^{-1})	*7689*	*19803*	*25800*
	band splitting (cm^{-1})	1110	2490	3000
	optical density (a.u.)	290	5260	2160
S25	energy (measured, cm^{-1})	8120	19230	26050
	energy (calculated, cm^{-1})	*7960*	*19023*	*25982*
	band splitting (cm^{-1})	1100	2580	2540
	optical density (a.u.)	390	5830	1670
S50	energy (measured, cm^{-1})	8120	19260	25860
	energy (calculated, cm^{-1})	*7780*	*19053*	*25851*
	band splitting (cm^{-1})	1080	2740	3000
	optical density (a.u.)	350	6370	2580
S75	energy (measured, cm^{-1})	8130	19310	25780
	energy (calculated, cm^{-1})	*7719*	*19128*	*25872*
	band splitting (cm^{-1})	1220	2370	3000
	optical density (a.u.)	80	2960	1430
S100	energy (measured, cm^{-1})	8080	19290	25850
	energy (calculated, cm^{-1})	*7854*	*19104*	*25967*
	band splitting (cm^{-1})	1060	2430	2900
	optical density (a.u.)	150	4600	1950

Table 4
Band energy, splitting and optical density of Cr^{3+} in octahedral coordination in the malayaite pigments. Electronic transition are referred to in both high symmetry (O_h) and actual point symmetry (C_i) notation.

sample	electronic transitions (O_h)	^2E_g (^2G)	$^2T_{1g}$ (^2G)	$^4T_{2g}$ (^4F)	$^4T_{1g}$ (^4F)
	electronic transitions (C_i)	^2A_g	$^2A_{1g}$	$^4A_{2g}$	$^4A_{1g}$
T18	energy (measured, cm^{-1})	11030	12990	17380	23260
	energy (calculated, cm^{-1})	*10511*	*11812*	*17360*	*23435*
	band splitting (cm^{-1})	650	780	1920	3000
	optical density (a.u.)	50	110	2000	4460
S18	energy (measured, cm^{-1})	10990	12960	17520	23040
	energy (calculated, cm^{-1})	*9980*	*11116*	*17510*	*23287*
	band splitting (cm^{-1})	730	920	2080	3000
	optical density (a.u.)	80	160	2440	4470
S25	energy (measured, cm^{-1})	11020	13020	17360	23590
	energy (calculated, cm^{-1})	*10999*	*12450*	*17370*	*23718*
	band splitting (cm^{-1})	820	910	2280	3000
	optical density (a.u.)	140	210	3250	5290
S50	energy (measured, cm^{-1})	11040	12920	17340	23140
	energy (calculated, cm^{-1})	*10508*	*11811*	*17330*	*23403*
	band splitting (cm^{-1})	620	610	2110	2850
	optical density (a.u.)	50	80	2456	4510
S75	energy (measured, cm^{-1})	11010	12990	17680	22910
	energy (calculated, cm^{-1})	*9448*	*10435*	*17670*	*23146*
	band splitting (cm^{-1})	540	1080	2130	3000
	optical density (a.u.)	20	130	1510	2650
S100	energy (measured, cm^{-1})	11050	13050	17590	23170
	energy (calculated, cm^{-1})	*10123*	*11293*	*17570*	*23429*
	band splitting (cm^{-1})	980	870	2050	3000
	optical density (a.u.)	121	140	2240	4260

Table 5
Crystal field strength 10Dq and Racah B parameter of malayaite pigments.

Chromophore	Optical parameters	T18	S18	S25	S50	S75	S100
Cr^{4+} (tetrahedral)	Crystal field strength 10Dq (cm^{-1})	10240	10090	10130	10160	10240	10100
	Racah B (cm^{-1})	393	396	403	398	376	396
	Nephelauxetic ratio β	0.39	0.39	0.40	0.39	0.37	0.39
Cr^{4+} (octahedral)	Crystal field strength 10Dq (cm^{-1})	20060	20270	20240	20250	20320	20310
	Racah B (cm^{-1})	552	527	545	533	529	538
	Nephelauxetic ratio β	0.54	0.52	0.54	0.53	0.52	0.53
Cr^{3+} (octahedral)	Crystal field strength 10Dq (cm^{-1})	17360	17510	17370	17330	17670	17570
	Racah B (cm^{-1})	585	549	618	585	514	558
	Nephelauxetic ratio β	0.64	0.60	0.67	0.64	0.56	0.61

Table 6
Metal-oxygen distances and site distortion in malayaite.

| M-O distance (Å)[1]		T18	S100	S50	S18	S75	S25
Ca-O1	[x1]	2.219(5)	2.229(4)	2.229(4)	2.221(5)	2.196(6)	2.216(5)
Ca-O2	[x2]	2.422(4)	2.409(4)	2.416(4)	2.416(4)	2.442(5)	2.422(4)
Ca-O3	[x2]	2.429(3)	2.426(3)	2.424(3)	2.431(3)	2.433(4)	2.433(3)
Ca-O3'	[x2]	2.735(4)	2.745(3)	2.741(3)	2.740(3)	2.739(4)	2.740(3)
Ca-O	mean	2.484	2.484	2.484	2.485	2.489	2.487
Sn-O1	[x2]	1.950(2)	1.948(1)	1.945(1)	1.951(2)	1.956(2)	1.953(2)
Sn-O2	[x2]	2.091(3)	2.097(3)	2.102(3)	2.092(3)	2.086(4)	2.085(3)
Sn-O3	[x2]	2.097(3)	2.103(3)	2.103(3)	2.096(3)	2.082(4)	2.091(3)
Sn-O	mean	2.046	2.049	2.050	2.046	2.041	2.043
Si-O2	[x2]	1.632(4)	1.627(4)	1.627(4)	1.637(4)	1.639(5)	1.645(4)
Si-O3	[x2]	1.646(4)	1.644(4)	1.638(3)	1.642(4)	1.647(5)	1.642(4)
Si-O	mean	1.639	1.636	1.632	1.640	1.643	1.644
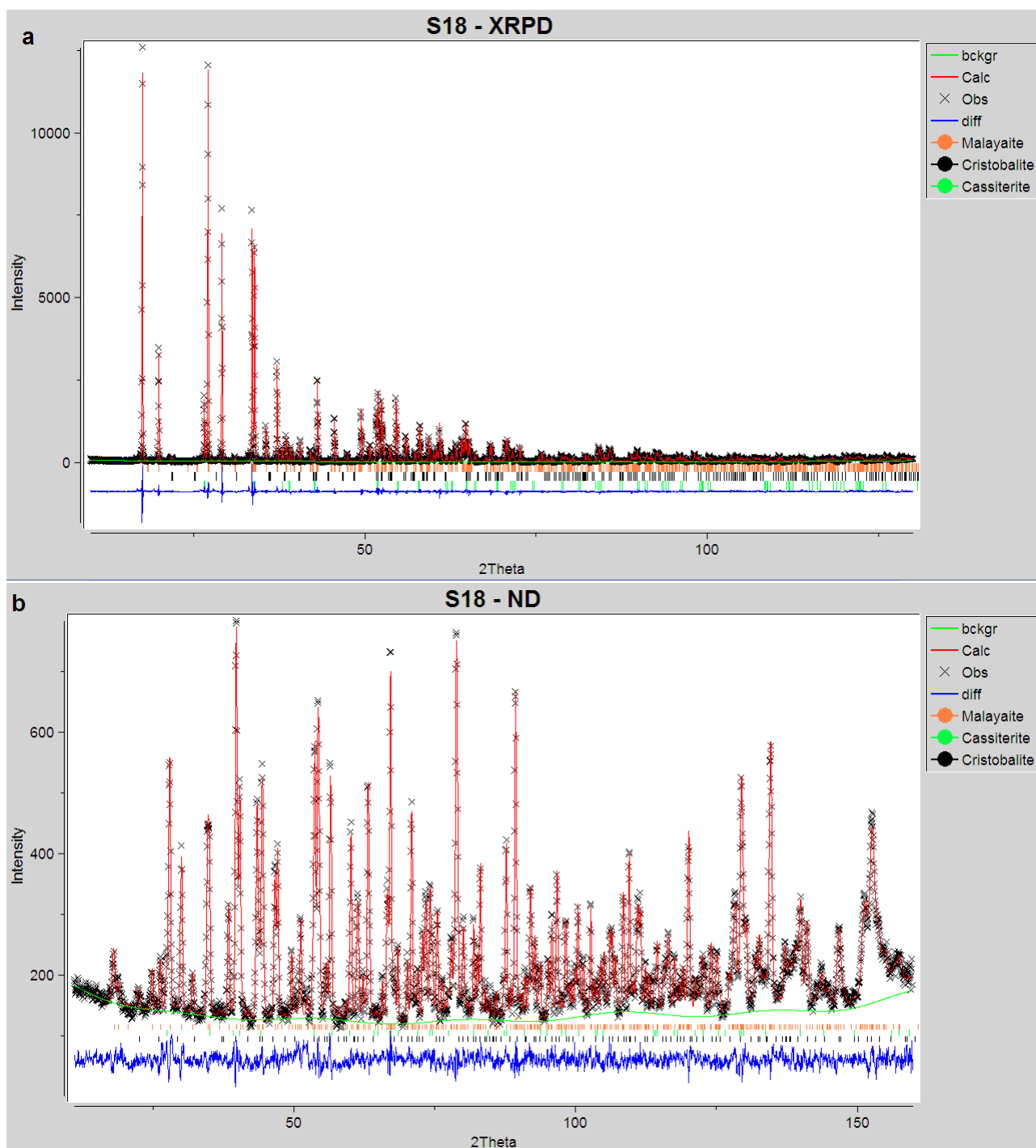
Fig. 1. Typical Rietveld plots (sample S18) of studied malayaite pigments for (a) X-ray and (b) neutron powder diffraction data.
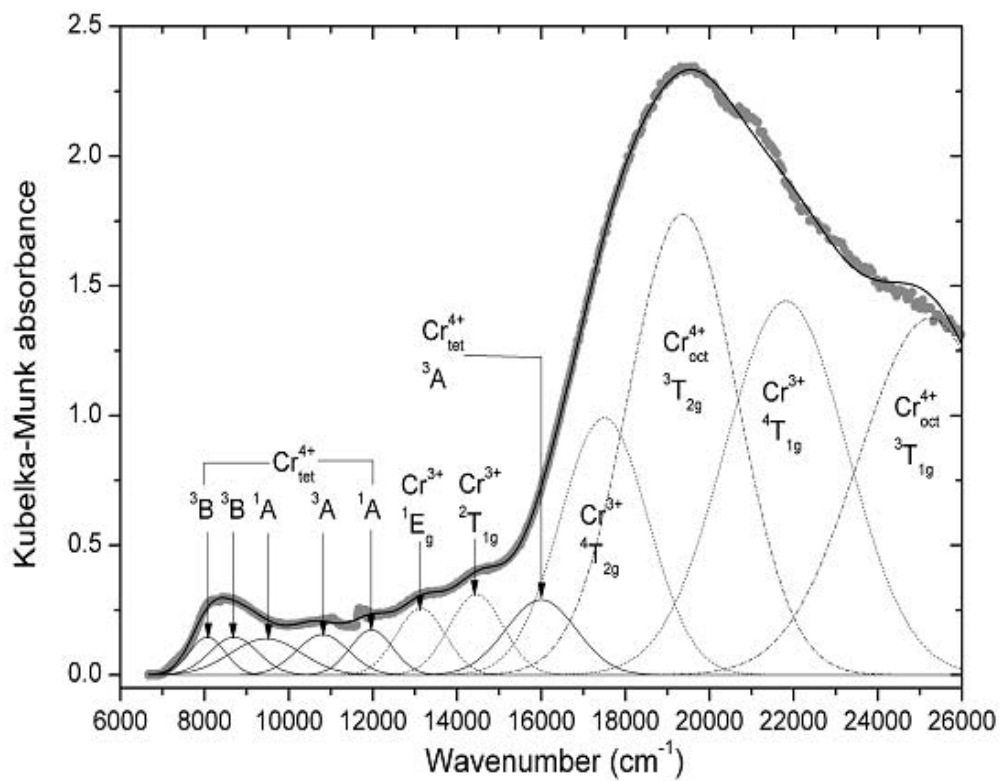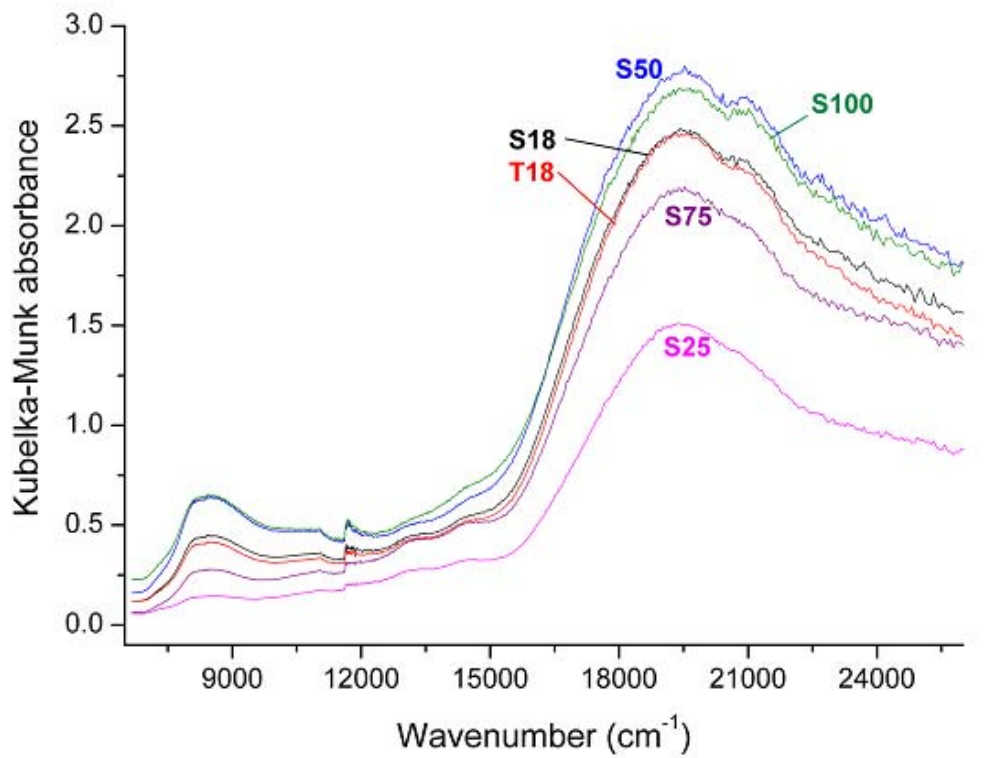
Fig. 2. Diffuse reflectance spectra of malayaites as measured for all samples (top) and as deconvoluted for sample T18 (bottom).
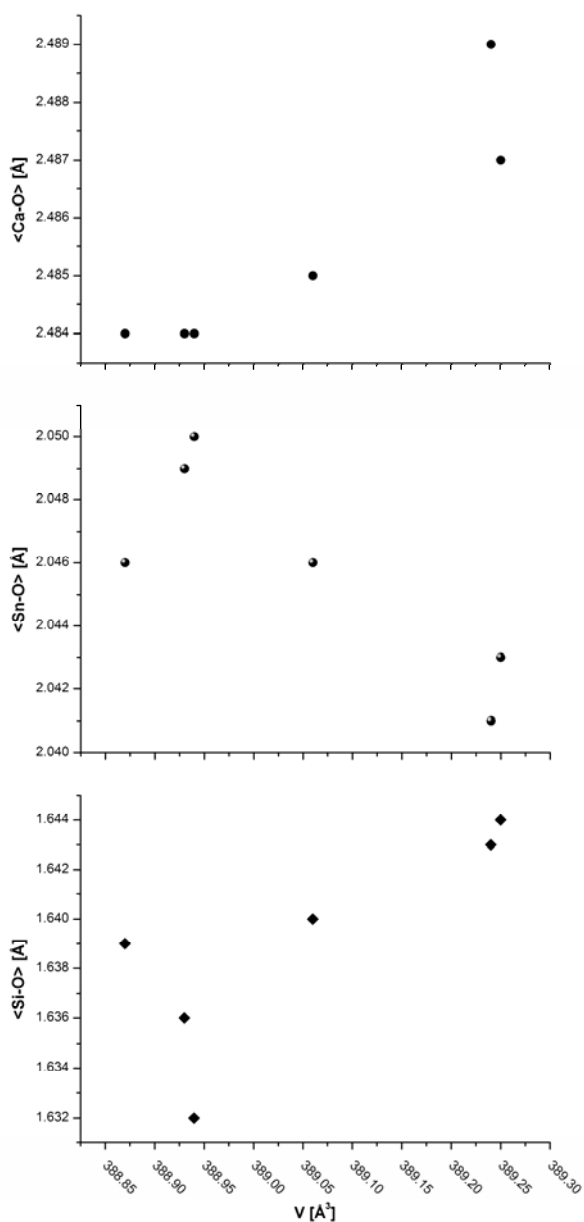
Fig. 3. Variation of mean Ca-, Sn-, and Si-oxygen distances vs. unit cell volume (inverse Cr content).
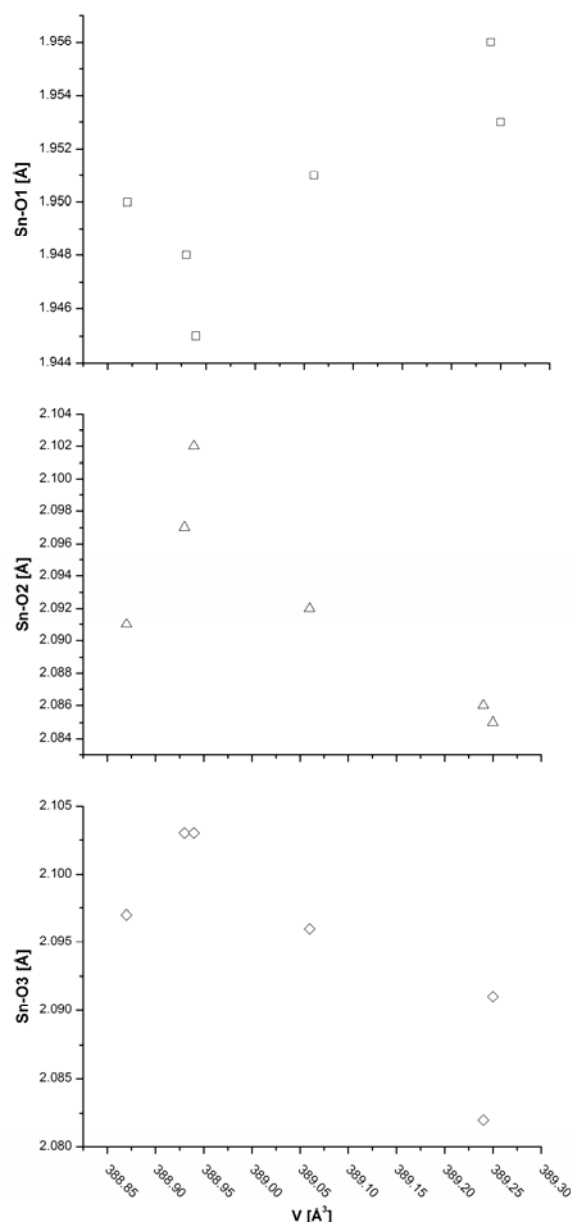

Fig. 4. Variation of individual Sn-O distances of SnO_6 octahedron as a function of cell volume.
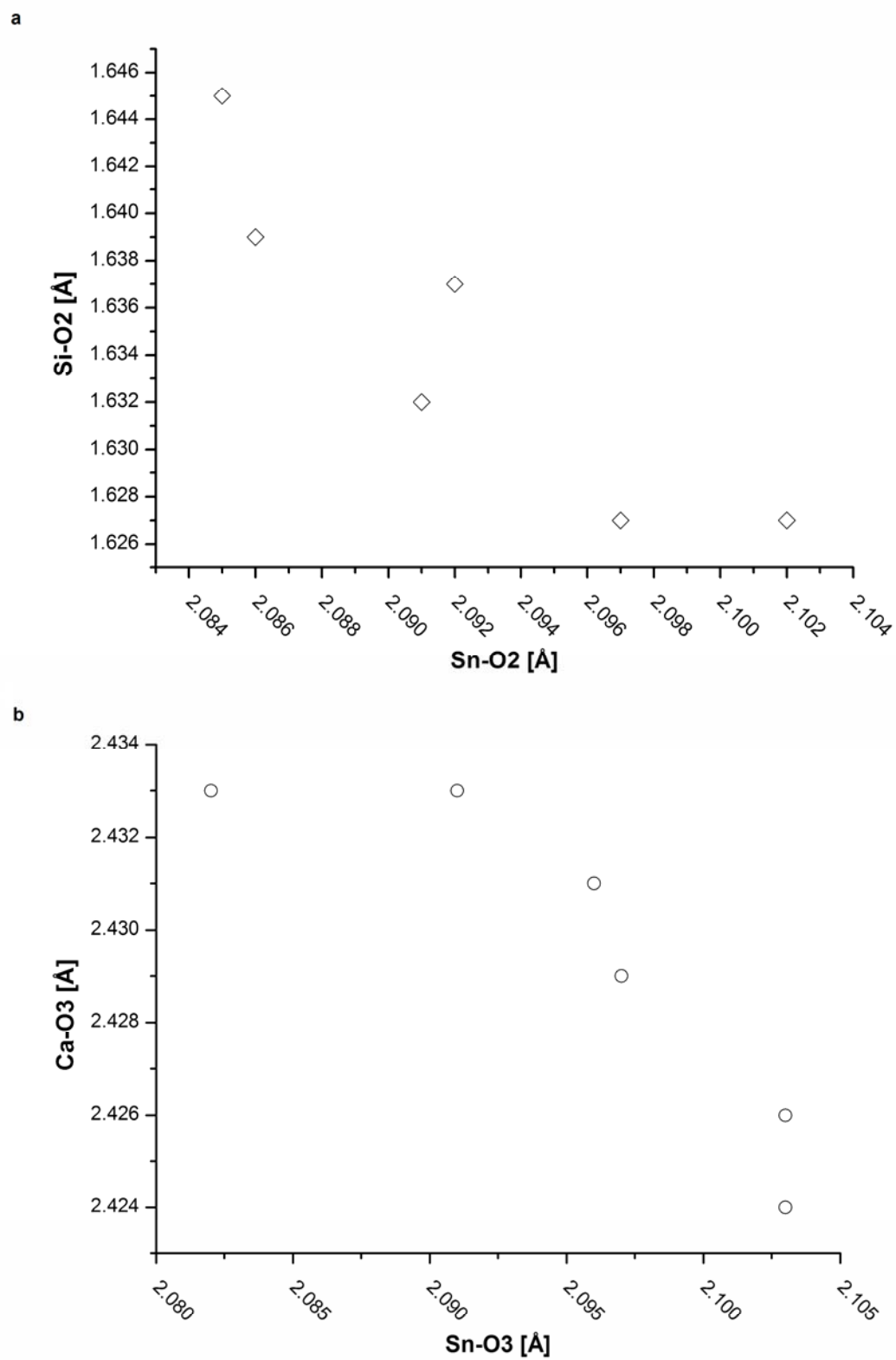
Fig. 5. Inverse relationships of Sn-O2 vs. Si-O2 (top) and Sn-O3 vs. Ca-O3 (bottom).